Copper-doped Bi_2MoO_6 with concurrent oxygen vacancies for enhanced CO_2 photoreduction

Jiawei Liu,[a] Xin Liu,[b] Chunhui Dai,[c] Chao Zeng,*[,a] Sajjad Ali,*[,d] Mohamed Bououdina,[d] Yushuai Jia*[,b]

[a] School of Chemical Engineering, Jiangxi Normal University, Nanchang 330022, PR China

[b] College of Chemistry and Materials, Jiangxi Normal University, Nanchang 330022, PR China

[c] Jiangxi Key Laboratory for Mass Spectrometry and Instrumentation, School of Chemistry, Biology, and Materials Science, East China University of Technology, Nanchang 330013, PR China

[d] Energy, Water, and Environment Lab, College of Humanities and Sciences, Prince Sultan University, Riyadh 11586, Saudi Arabia

E-mail*: czeng@jxnu.edu.cn; sajjad@alum.imr.ac.cn; ysjia@jxnu.edu.cn*

1. Computational section

1.1 Computational setup

Theoretical calculations were conducted using spin-polarized density functional theory (DFT) implemented through the Vienna ab initio simulation package (VASP).[1] The Perdew-Burke-Ernzerhof (PBE) functional,[2] a type of generalized gradient approximation (GGA), was employed to calculate the exchange-correlation potentials. A 4×2×2 k-points grid and an energy cutoff of 450 eV were employed for structural relaxation. Ionic relaxations were conducted with conventional energy criteria (10^{-5} eV), while force convergence thresholds were set at -0.02 eVÅ^{-1} during optimization. Based on experimental findings, a 131 facet of Bi_2MoO_6 was selected as a representative model for CO_2 reduction. To minimize periodic image interactions, the separation between adjacent cells was adjusted to approximately 15 Å. Gas-phase molecule energies (H_2, H_2O, and CO_2) were evaluated within a box measuring 27 Å × 27 Å × 20 Å. Charge population and transfer were determined using the Bader method.[3]

The conversion of CO_2 to CO through photo-reduction occurs through a mechanism involving the transfer of two electrons, consisting of two elementary steps coupled with proton-electron interactions:

$$* + CO_{2(g)} + 2(H^+ + e^-) \rightarrow *COOH + H^+ + e^- \quad (1)$$

$$*COOH + H^+ + e^- \rightarrow *CO + H_2O_{(l)} \quad (2)$$

$$*CO \rightarrow CO_{(g)} + * \quad (3)$$

Additionally, the *CO that has been adsorbed can undergo further reduction to *CHO and CH_4 via eight-electron CO_2 reduction products, following the subsequent route;

$$*CO + H^+ + e^- \rightarrow *CHO \quad (4)$$

$$*CHO + H^+ + e^- \rightarrow CH_2O* \quad (5)$$

$$*OCH_2 + H^+ + e^- \rightarrow CH_3O* \quad (6)$$

$$*OCH_3 + H^+ + e^- \rightarrow *O + CH_{4(g)} \quad (7)$$

$$*O + H^+ + e^- \rightarrow *OH \quad (8)$$

$$*OH + H^+ + e^- \rightarrow H_2O_{(l)} + * \quad (9)$$

where "*" denoted the active site of catalysts, (g) denoted gas phase, respectively, and $HCOOH*$, $*COOH$, $*CO$, $*CHO$, CH_2O*, CH_3O*, and $*OH$, are the adsorbed intermediates.

The addition of corrections for zero-point energy, entropy, and enthalpy was performed on adsorbates to transform electronic energy into free energy.

The Gibbs free energy (G) at 0 V was modified by equation (10).

$$G = E_{DFT} + E_{ZPE} - TS + \int C_p dT \quad (10)$$

where E_{DFT}, E_{ZPE}, TS, and $\int C_p dT$ denoted electronic energy obtained from DFT optimization, zero-point vibrational energy, entropy, and heat capacity at room temperature (T=298.15 K), respectively. The computational hydrogen electrode (CHE) model was used to calculate the Gibbs free energy for the reaction step involving the coupled of proton-electron, in which the free energy of a pair of proton and electron ($H^+ + e^-$) was calculated as a function of applied potential relative to a reversible hydrogen electrode (U *vs* RHE), i.e., $\mu(H^+) + \mu(e^-) = \frac{1}{2}\mu(H_2) - eU$.[4] The reaction free energies of each elementary reaction ($-\Delta G$) at a given potential U_{RHE} are calculated as:

$$\Delta G = \mu(\text{product}) - \mu(\text{reactant}) - \frac{1\mu(H2)}{2} - eU_{RHE} \quad (11)$$

Where μ was the chemical potential. Precisely, when U=0 V then,

$$\Delta G = -U_L \times e \quad (12)$$

Where U_L was the limiting potential, and U_L of each specific product (CO, CH_4 and H_2O) were obtained via $U_L = -\Delta G_{max}/e$, where (ΔG_{max}) was the maximum free energy change and determined the value of potential-determining step.

Charge transfer Δρ from the atoms to the crystal is calculated by,

$$\Delta\rho = \rho(\text{crystal}) - \rho(\text{atoms}) \tag{13}$$

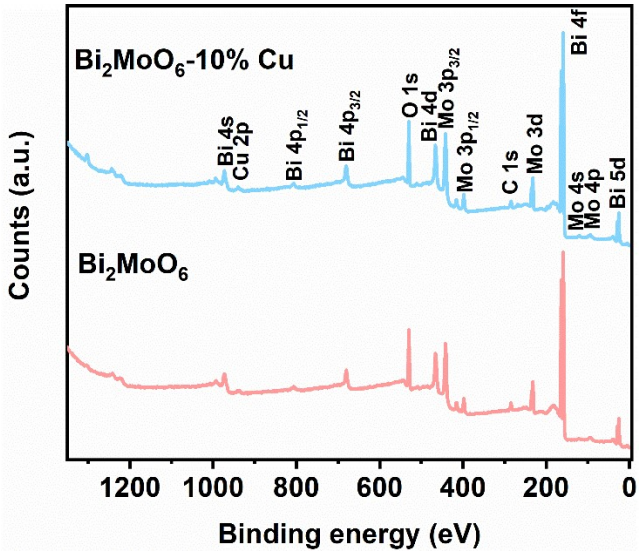

Figure S1. Typical XPS survey spectra of Bi_2MoO_6 and Bi_2MoO_6-10% Cu.

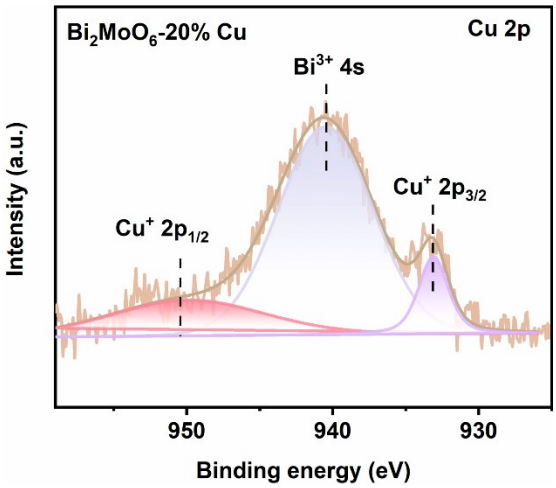

Figure S2. High-resolution XPS spectrum of Cu 2p for Bi_2MoO_6-20% Cu.

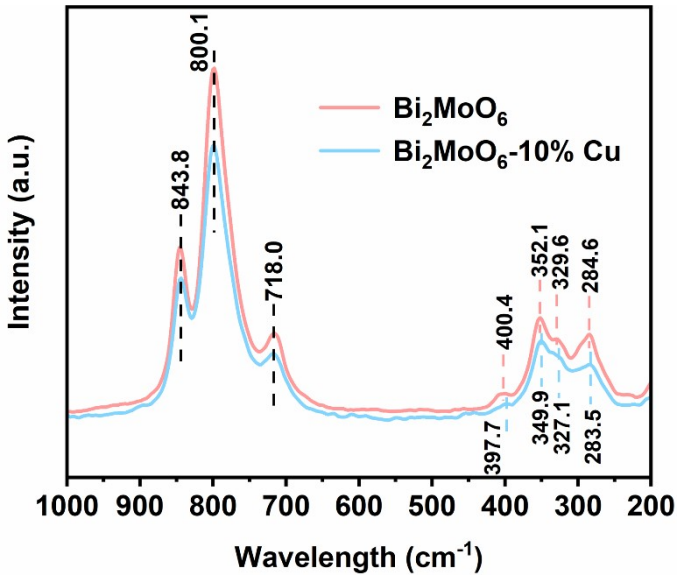

Figure S3. Raman spectra of Bi_2MoO_6 and Bi_2MoO_6-10% Cu.

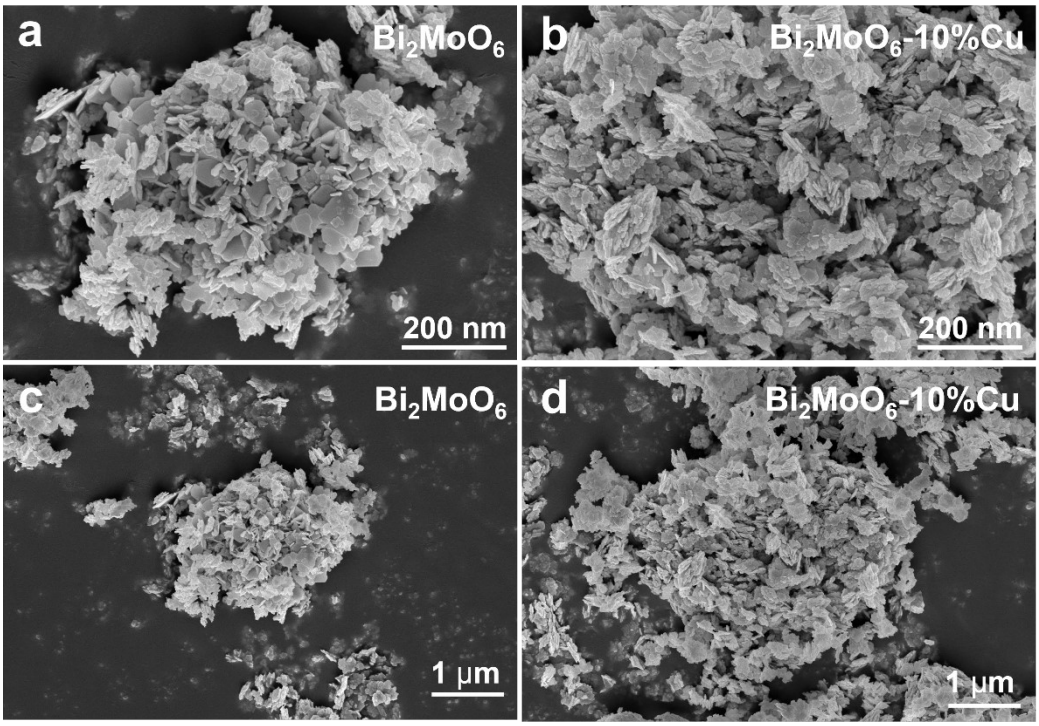

Figure S4. SEM images of (a, c) Bi_2MoO_6, and (b, d) Bi_2MoO_6-10% Cu.

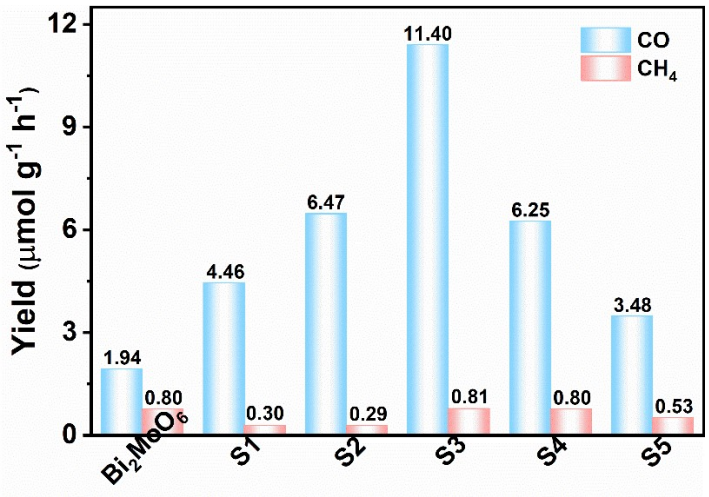

Figure S5. The yield of photocatalytic CO_2 conversion products of Bi_2MoO_6 and Bi_2MoO_6-XCu (S1-S5: X=1%, 5%, 10%, 15% and 20%).

Table S1. Bi_2MoO_6-10% Cu photocatalyst and other reported photocatalysts towards photocatalytic CO evolution rate from CO_2 reduction.

Photocatalyst	Light source	Activity, μmol g^{-1} h^{-1}	Selectivity, %	Ref
Bi_2MoO_6-10% Cu	300 W Xe lamp	11.40	69.3	--
Co-POR	300 W Xe lamp	0.40	--	5
$Bi_{24}O_{31}Cl_{10}$-O_V	300 W Xe lamp	0.9	--	6
2H/3C-SiC	300 W Xe lamp	4.68	--	7
3D $CoAl_2O_4$	300 W Xe lamp	4.73	--	8
LHTO nanosheets	300 W Xe lamp	4	93	9
CdG-2	350 W Xe lamp	2.59	--	10
Bi_2MoO_6 nanosheets	300 W Xe lamp	3.62	--	11
Au–BiOCl-OV	300 W Xe lamp	4.85	--	12
BON-Br	150 W Xe lamp	8.12	--	13
5 wt.% GO/TiO_2	500 W Xe lamp	1.86	--	14
CdS/$CdWO_4$	300 W Xe lamp	1.4	--	15
ultrathin ZnAl LDH	300 W Xe lamp	7.6	--	16
ISS/CBB	300 W Xe lamp	9.55	92.9	17
BOC-OV	300 W Xe lamp	4.19	＞90	18

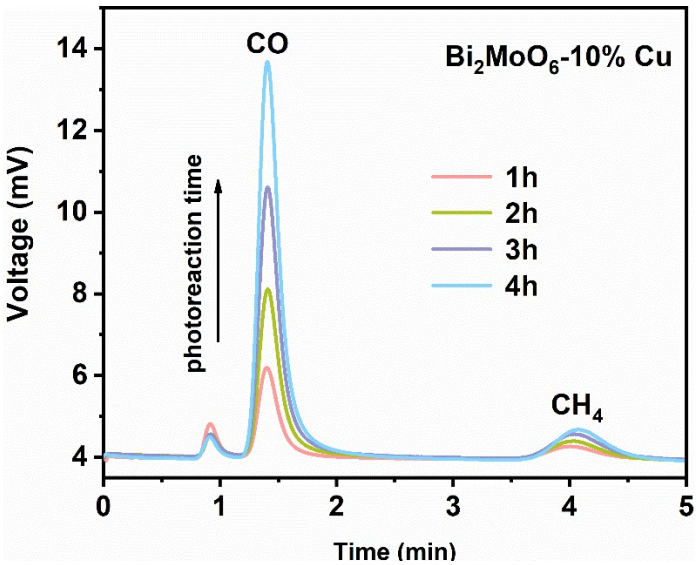

Figure S6. Original gas chromatograms of the gas products for CO_2 reduction over Bi_2MoO_6-10% Cu under different irradiation times.

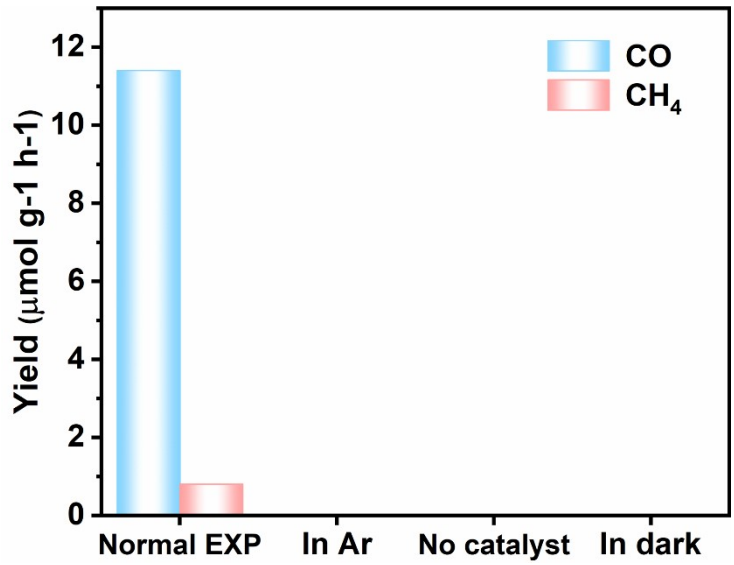

Figure S7. CO_2 photoreduction activity under various conditions.

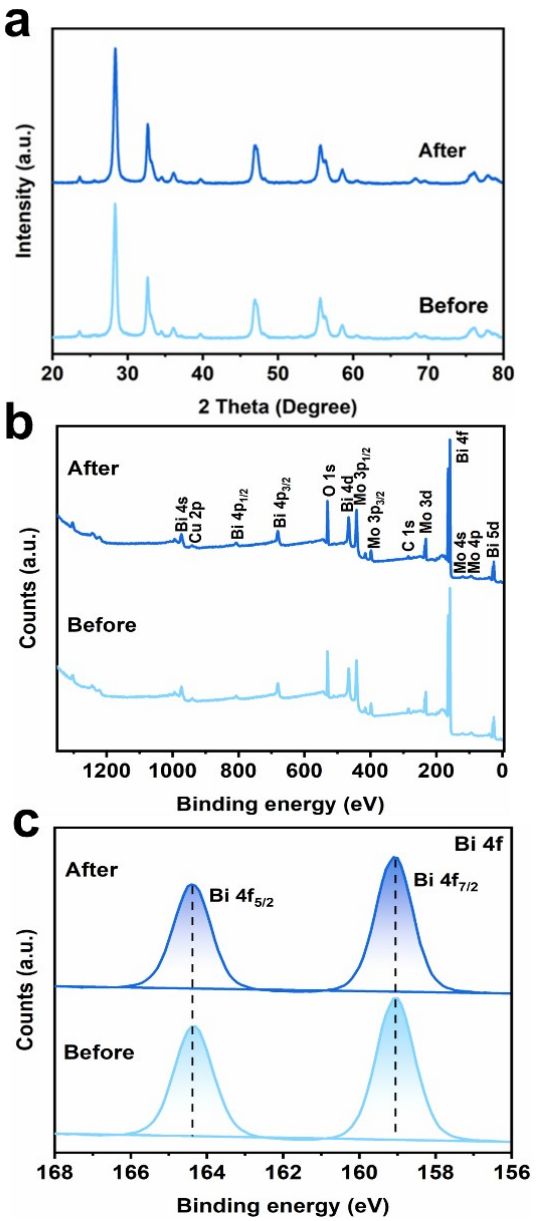

Figure S8. (a) XRD patterns, (b) typical XPS survey spectra, and (c) high-resolution XPS spectra of Bi 4f for Bi_2MoO_6-10% Cu before and after cycling reactions.

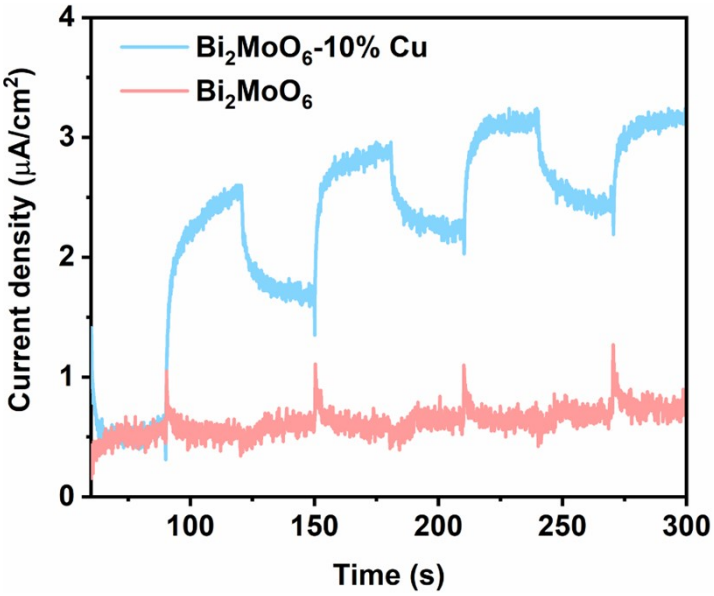

Figure S9. Transient photocurrent responses for Bi_2MoO_6 and Bi_2MoO_6-10% Cu.

Table S2 The fitted parameters of the equivalent circuit of Bi_2MoO_6 and Bi_2MoO_6-10% Cu in the EIS spectra.

Sample	Element	Parameter	Value (Ω)	Estimated Error (%)
Bi_2MoO_6	Rs	R	33.8100	0.7333
	Rct	R	2.3730E+11	1.0577E8
	CPE-T	Y0	4.4333E-5	1.9591
	CPE-P	N	0.9537	0.4115
Bi_2MoO_6-10% Cu	Rs	R	41.0	0.7305
	Rct	R	1368	2.2531
	CPE-T	Y0	6.7246E-5	2.9649
	CPE-P	N	0.8842	0.6538

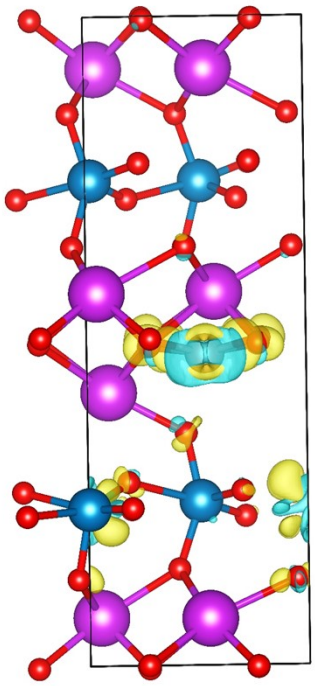

Figure S10. Charge density difference plot of Cu/Ov-Bi_2MoO_6. The yellow and sky-blue color loops represent charge accumulation and depletion regions. The isosurface value is set to 0.002 e/Bohr³.

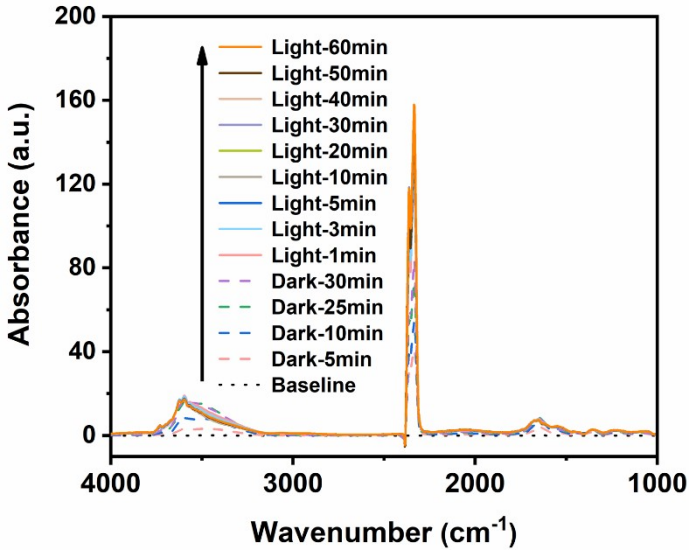

Figure S11. In situ FT-IR spectra of Bi_2MoO_6-10% Cu in dark and under irradiation.

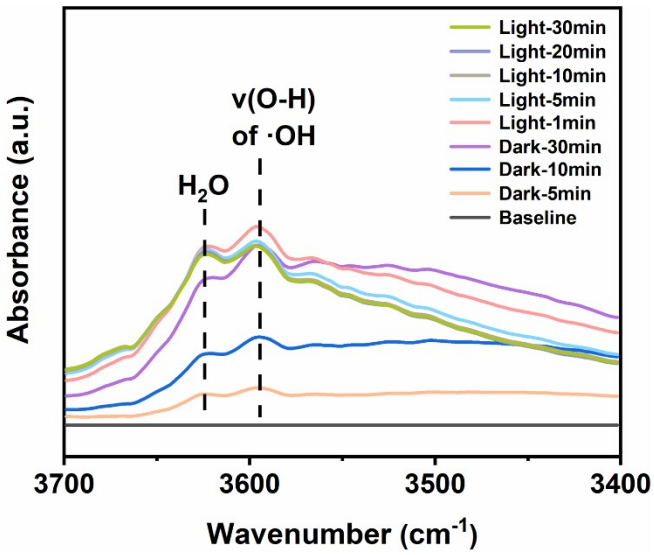

Figure S12. The zoomed view of the in situ FTIR spectra of Bi_2MoO_6-10% Cu in the region of 3400-3700 cm^{-1}.

Table S3 Summary of simulation parameters obtained from DFT calculation. The DFT energies (E_{DFT}), zero-point energies (E_{ZPE}), entropies (TS), and free energy correction (G_{corr}) for the gas molecules. The values are measured in eV. The vibrational corrections for gas molecules are taken from ref.[19,20]

Species	E_{DFT}	E_{ZPE}	**TS**	G_{corr}
H_2	-6.77	0.27	0.4	-6.9
CO_2	-22.9	0.31	0.4	-23.31
$HCOOH$	-29.88	0.89	0.66	-29.99
CO	-14.78	0.14	0.98	-14.31
H_2O	-14.22	0.57	0.61	-14.32
CH_4	-24.04	1.2	0.6	-23.44

Table S4 Summary of simulation parameters obtained from DFT calculation. The DFT energies (E_{DFT}), zero-point energies (E_{ZPE}), heat capacity ($\int C_p dT$) entropies (TS), and free energy correction (G_{corr}) and free energy (ΔG) for intermediates involved in CO_2 photoreduction reaction on pristine Bi_2MoO_6. The values are measured in eV.

Number	Species	E_{DFT}	E_{ZPE}	$\int C_p dT$	TS	G_{corr}	ΔG	ΔG_n
0	$*$	-677.776	0.00	0.00	0.00	-677.776	0.00	0.00
1	$*COOH$	-703.973	0.604	0.111	0.236	-703.494	0.723	0.723
2	$*CO$	-692.927	0.135	0.024	0.035	-692.803	-0.18	0.543
3	$*CHO$	-696.353	0.448	0.064	0.127	-695.969	0.284	0.827
4	CH_2O*	-700.114	0.758	0.112	0.241	-699.485	-0.066	0.761
5	CH_3O*	-704.514	1.093	0.097	0.194	-703.518	-0.583	0.178
6	$*O+CH_4$	-707.693	1.218	0.100	0.225	-706.599	0.369	0.547
7	$*OH$	-688.668	0.345	0.056	0.105	-688.372	-1.762	-1.215
8	$*+H_2O$	-692.228	0.631	0.100	0.214	-691.712	0.120	-1.106

Table S5 Summary of simulation parameters obtained from DFT calculation. The DFT energies (E_{DFT}), zero-point energies (E_{ZPE}), heat capacity ($\int C_p dT$) entropies (TS), and free energy correction (G_{corr}) and free energy (ΔG) for intermediates involved in CO_2 photoreduction reaction on Cu/Ov-Bi_2MoO_6. The values are measured in eV.

Number	Species	E_{DFT}	E_{ZPE}	$\int C_p dT$	TS	G_{corr}	ΔG	ΔG_n
0	$*$	-675.093	0.00	0.00	0.00	-675.093	0.00	0.00
1	$*COOH$	-701.679	0.594	0.111	0.235	-701.208	0.325	0.325
2	$*CO$	-690.915	0.202	0.071	0.146	-690.788	-0.450	-0.125
3	$*CHO$	-693.577	0.140	0.067	0.431	-693.801	0.437	0.311
4	CH_2O*	-697.565	0.760	0.075	0.137	-696.867	0.384	0.695
5	CH_3O*	-701.623	1.061	0.098	0.194	-700.657	-0.340	-0.355
6	$*O+CH_4$	-706.037	1.267	0.099	0.229	-704.900	-0.793	-0.438
7	$*OH$	-685.269	0.328	0.044	0.082	-684.979	-0.069	-0.506
8	$*+H_2O$	-689.205	0.591	0.071	0.150	-688.693	-0.264	-0.770

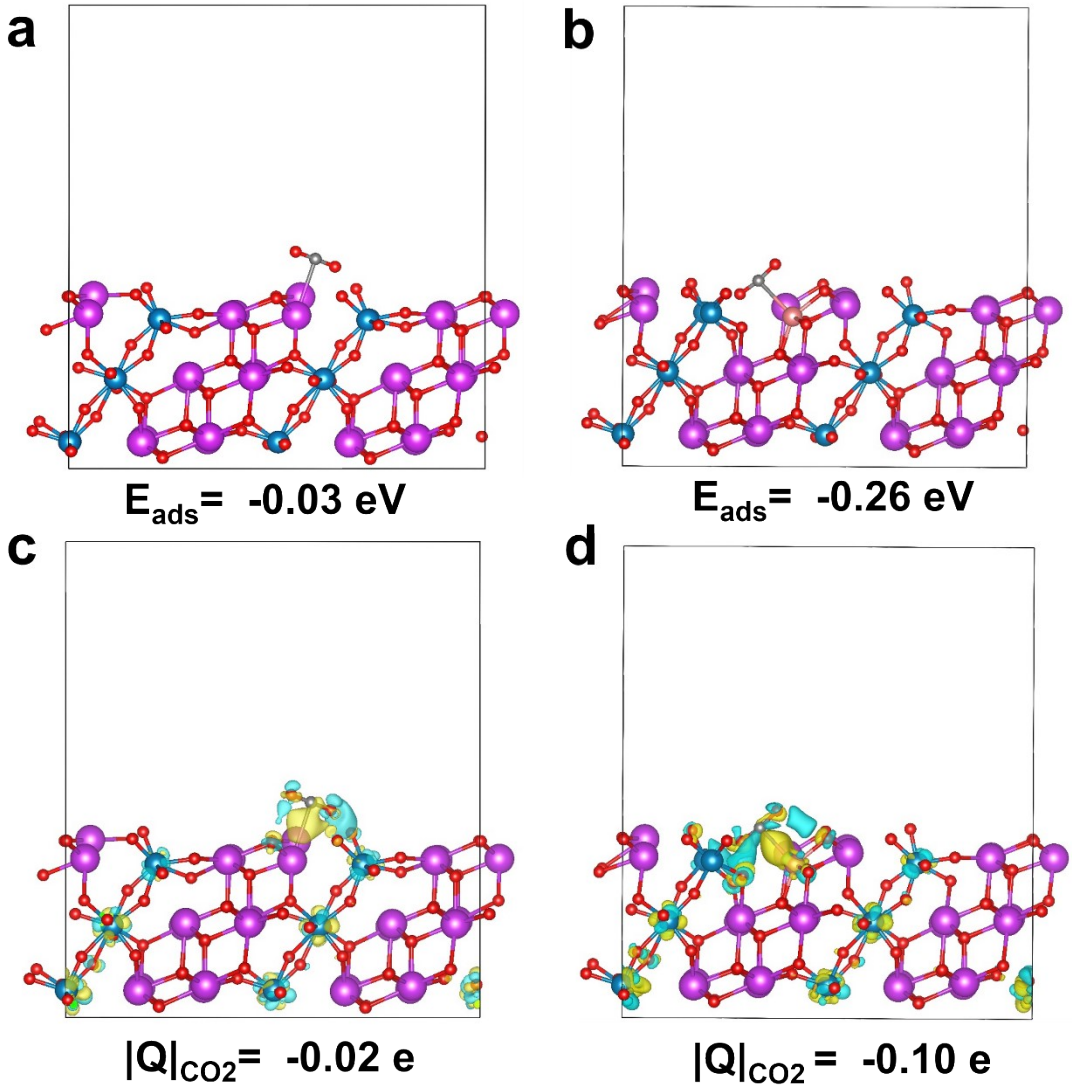

Figure S13. The optimized structure along charge density difference plot of CO_2 adsorption (a, c) pure Bi_2MoO_6, (b, d) Cu/Ov-Bi_2MoO_6 respectively. The yellow and sky green color loops represent charge accumulation and depletion region. The isosurface value is set to 0.004 e/Bohr³.

References

1. G. Kresse and J. Furthmüller, Efficient iterative schemes for total-energy calculations using a plane-wave basis set, *Phys. Rev. B*, 1996, **54**, 11169-11186.
2. J. P. Perdew, A. Ruzsinszky, G. I. Csonka, O. A. Vydrov, G. E. Scuseria, L. A. Constantin, X. L. Zhou and K. Burke, Restoring the density-gradient expansion for exchange in solids and surfaces, *Phys. Rev. Lett.*, 2008, **100**, 136406.
3. G. Henkelman, A. Arnaldsson and H. Jónsson, A fast and robust algorithm for Bader decomposition of charge density, *Comput. Mater. Sci.*, 2006, **36**, 354-360.
4. J. K. Norskov, J. Rossmeisl, A. Logadottir, L. Lindqvist, J. R. Kitchin, Bligaard and T. H. Jónsson, Origin of the overpotential for oxygen reduction at a fuel-cell cathode, *J. Phys. Chem. B*, 2004, **108**, 17886-17892.
5. J. Xu, X. W. Liu, Z. J. Zhou and M. H. Xu, Photocatalytic CO_2 reduction catalyzed by metalloporphyrin: Understanding of cobalt and nickel sites in activity and adsorption, *Appl. Surf. Sci.*, 2020, **513**, 145801.
6. X. L. Jin, C. D. Lv, X. Zhou, L. Q. Ye, H. Q. Xie, Y. Liu, H. Su, B. Zhang and G. Chen, Oxygen vacancy engineering of $Bi_{24}O_{31}Cl_{10}$ for boosted photocatalytic CO_2 conversion, *ChemSusChem*, 2019, **12**, 2740-2747.
7. Y. Z. Liu, B. Wang, D. M. Li, J. N. Shen, Z. Z. Zhang and X. X. Wang, Fabrication of 2H/3C-SiC heterophase junction nanocages for enhancing photocatalytic CO_2 reduction, *J. Colloid Interf. Sci.*, 2022, **622**, 31-39.
8. F. Lv, W. Y. Zhang, L. He, X. Bai, Y. Song and Y. Zhao, 3D porous flower-like $CoAl_2O_4$ to boost the photocatalytic CO_2 reduction reaction, *J. Mater. Chem. A*,

2023, **11**, 2826-2835.

9. J. Y. Xue, Y. Yu, C. Yang, K. F. Zhang, X. W. Zhan, J. M. Song, J. J. Gui, Y. K. Li, X. Jin, S. Gao and Y. Xie, Developing atomically thin $Li_{1.81}H_{0.19}Ti_2O_5 \cdot 2H_2O$ nanosheets for selective photocatalytic CO_2 reduction to CO, *Langmuir*, 2022, **38**, 523-530.
10. C. B. Bie, B. C. Zhu, F. Y. Xu, L. Y. Zhang and J. G. Yu, In situ grown monolayer n-doped graphene on CdS hollow spheres with seamless contact for photocatalytic CO_2 reduction, *Adv. Mater.*, 2019, **31**, 1902868.
11. J. Di, X. X. Zhao, C. Lian, M. X. Ji, J. X. Xia, J. Xiong, W. Zhou, X. Z. Cao, Y. B. She, H. L. Liu, K. Loh, S. J. Pennycook, H. M. Li and Z. Liu, Atomically-thin Bi_2MoO_6 nanosheets with vacancy pairs for improved photocatalytic CO_2 reduction, *Nano Energy,* 2019, **61**, 54-59.
12. Y. L. Li, Y. Liu, H. Y. Mu, R. H. Liu, Y. J. Hao, X. J. Wang, D. Hildebrandt, X. Y. Liu and F. T. Li, The simultaneous adsorption, activation and in situ reduction of carbon dioxide over Au-loading BiOCl with rich oxygen vacancies, *Nanoscale*, 2021, **13**, 2585-2592.
13. L. Hao, L. Kang, H. W. Huang, L. Q. Ye, K. L. Han, S. Q. Yang, H. J. Yu, M. Batmunkh, Y. H. Zhang and T. Y. Ma, Surface-halogenation-induced atomic-site activation and local charge separation for superb CO_2 photoreduction, *Adv. Mater.*, 2019, **31**, 1900546.
14. L. L. Tan, W. J. Ong, S. P. Chai and A. R. Mohamed, Photocatalytic reduction of CO_2 with H_2O over graphene oxide supported oxygen-rich TiO_2 hybrid

photocatalyst under visible light irradiation: Process and kinetic studies, *Chem. Eng. J.*, 2017, **308**, 248-255.

15. Y. Y. Li, Z. H. Wei, J. B. Fan, Z. J. Li and H. C. Yao, Photocatalytic CO_2 reduction activity of Z-scheme CdS/$CdWO_4$ catalysts constructed by surface charge directed selective deposition of CdS, *Appl. Surf. Sci.*, 2019, **483**, 442-452.
16. Y. F. Zhao, G. B. Chen, T. Bian, C. Zhou, G. I. N. Waterhouse, L. Z. Wu, C. H. Tung, L. J. Smith, D. O'Hare and T. R. Zhang, Defect- rich ultrathin ZnAl-layered double hydroxide nanosheets for efficient photoreduction of CO_2 to CO with water, *Adv. Mater.*, 2015, **27**, 7824-7831.
17. Z. Z. Zhang, M. Y. Wang, Z. X. Chi, W. J. Li, H. Yu, N. Yang and H. B. Yu, Internal electric field engineering step-scheme-based heterojunction using lead-free Cs3Bi2Br9 perovskite-modified In4SnS8 for selective photocatalytic CO_2 reduction to CO, *Appl. Catal. B-Environ.*, 2022, **313**, 121426.
18. Z. Ma, P. Li, L. Ye, Y. Zhou, F. Su, C. Ding, H. Xie, Y. Bai and P. K. Wong, Oxygen vacancies induced exciton dissociation of flexible BiOCl nanosheets for effective photocatalytic CO_2 conversion, *J. Mater. Chem. A*, 2017, **5**, 24995-25004.
19. A. A. Peterson, F. Abild-Pedersen, F. Studt, J. Rossmeisl and J. K. Norskov, How copper catalyzes the electroreduction of carbon dioxide into hydrocarbon fuels, *Energy Environ. Sci.*, 2010, **3**, 1311-1315.
20. W. C. Ma, S. J. Xie, X. G. Zhang, F. F. Sun, J. C. Kang, Z. Jiang, Q. H. Zhang,

D. Y. Wu and Y. Wang, Promoting electrocatalytic CO_2 reduction to formate via sulfur-boosting water activation on indium surfaces, *Nat. Commun.*, 2019, **10**, 892.